JGR Oceans

RESEARCH ARTICLE
10.1029/2020JC016996

Time Dependent Flow of Atlantic Water on the Continental Slope of the Beaufort Sea Based on Moorings

Jianqiang Li[1], Peigen Lin[2], Robert S. Pickart[2], and Xiao-Yi Yang[1,3]

[1]State Key Laboratory of Marine Environmental Science, and College of Ocean and Earth Sciences, Xiamen University, Xiamen, China, [2]Woods Hole Oceanographic Institution, Woods Hole, MA, USA, [3]Southern Marine Science and Engineering Guangdong Laboratory (Zhuhai), Zhuhai, China

Abstract The flow and transformation of warm, salty Atlantic-origin water (AW) in the Arctic Ocean plays an important role in the global overturning circulation that helps regulate Earth's climate. The heat that it transports also impacts ice melt in different parts of the Arctic. This study uses data from a mooring array deployed across the shelf/slope of the Alaskan Beaufort Sea from 2002–2004 to investigate the flow of AW. A short-lived "rebound jet" of AW on the upper continental slope regularly follows wind-driven upwelling events. A total of 57 such events, lasting on average 3 days each, occurred over the 2 year period. As the easterly wind subsides, the rebound jet quickly spins up while the isopycnals continue to slump from their upwelled state. The strength of the jet is related to the cross-slope isopycnal displacement, which in turn is dependent on the magnitude of the wind, in line with previous modeling. Seaward of the rebound jet, the offshore-most mooring of the array measured the onshore branch of the AW boundary flowing eastward in the Canada Basin. However, the signature of the boundary current was only evident in the second year of the mooring timeseries. We suspect that this is due to the varying influence of the Beaufort Gyre in the two years, associated with a change in pattern of the wind stress curl that helps drive the gyre.

Plain Language Summary The flow and transformation of warm, salty Atlantic-origin water (AW) in the Arctic Ocean plays an important role in the global overturning circulation that helps regulate Earth's climate. The heat that it transports also impacts ice melt in different parts of the Arctic. This study uses two years of mooring data across the continental shelf and slope of the Alaskan Beaufort Sea to investigate the time-dependent flow of AW. Short-lived bursts of AW, known as "rebound jets", occur following easterly wind storms throughout the year. Our measurements support the dynamical explanation for the events previously deduced from numerical modeling. Farther offshore, the mooring array measured one of the branches of the AW boundary current in the Canada Basin. The signature of this flow appears to vary according to the rotation of winds over the basin, which helps drive the Beaufort Gyre. Our results imply a dynamical connection between the gyre and the boundary current, motivating further study.

Key Points:

- A short-lived "rebound jet" of Atlantic Water (AW) on the upper slope regularly follows wind-driven upwelling events in the Beaufort Sea
- A total of 57 such events, lasting on average 3 days each, occurred over the 2 year measurement period
- The onshore branch of the AW boundary current is impacted by local wind stress as well as wind stress curl in the Canada Basin

Correspondence to:
R. S. Pickart,
rpickart@whoi.edu

Citation:
Li, J., Lin, P., Pickart, R. S., & Yang, X.-Y. (2021). Time dependent flow of Atlantic Water on the continental slope of the Beaufort Sea based on moorings. *Journal of Geophysical Research: Oceans*, *126*, e2020JC016996. https://doi.org/10.1029/2020JC016996

Received 17 NOV 2020
Accepted 24 MAY 2021

1. Introduction

Warm, salty Atlantic Water (AW) is a ubiquitous feature of the middepth Arctic Ocean. It enters the Arctic through the eastern side of Fram Strait and via the Barents Sea, and circulates cyclonically through the different basins as a boundary current before exiting the western side of Fram Strait (e.g., Aksenov et al., 2011). During its long transit the water is cooled, freshened and densified. After re-entering the Nordic Seas, the modified water flows southward with the East Greenland Current and participates in the dense overflow through Denmark Strait (Mauritzen, 1996). Hence, the transformation of AW in the Arctic can be thought of as the northern headwaters of the Atlantic Meridional Overturning Circulation, and thus represents an important component of our global climate system. The AW strongly influences the water column structure throughout the Arctic, contributing to the maintenance of the halocline. The layer also contains a vast amount of heat that has been shown to influence ice melt in the Eurasian Basin (Polyakov et al., 2017) and along the southern margin of the Canada Basin (Ladd et al., 2016).

To first order, the flow of AW is steered by bathymetry (e.g., Aksenov et al., 2011; Rudels et al., 1994; see Figure 1a). The water emanating from Fram Strait splits into three different branches in the northern part

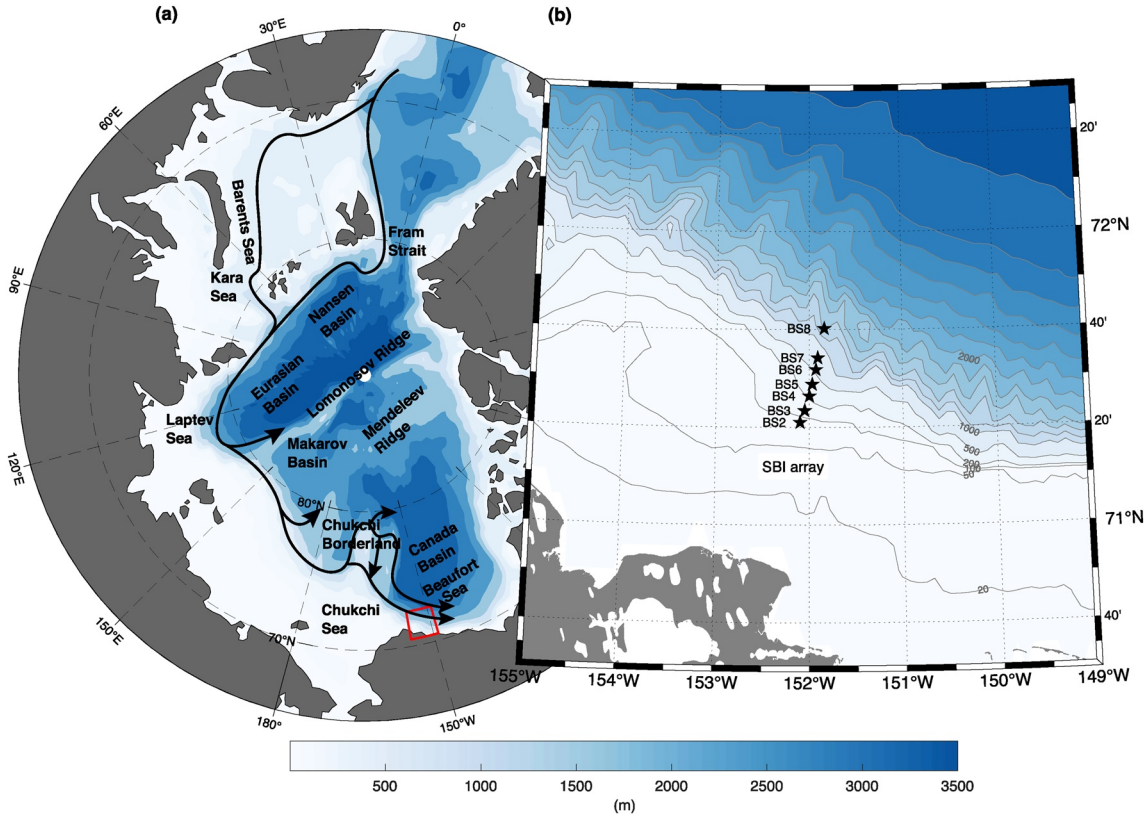

Figure 1. (a) Schematic circulation of the Atlantic Water (black arrows) and relevant place names. The shaded bathymetry is from IBCAO v3. The red box is the area enlarged in (b), which is the domain considered in the present study. (b) Moorings comprising the two-year shelf basin interaction mooring array (black stars).

of the strait: the Yermak Plateau branch (Meyer et al., 2017), the Yermak Pass Branch (Koenig et al., 2017), and the Svalbard slope branch (Cokelet et al., 2008; Kolas & Fer, 2018; Pérez-Hernández et al., 2017; Våge et al, 2016). These branches are believed to subsequently merge back into a single boundary along the northern continental slope of Svalbard. Using data from a year-long mooring array at this location, Pérez-Hernández et al. (2019) determined that the AW occupies the depth range 150–600 m and estimated its transport within the boundary current to be 2.08 ± 0.24 Sv.

Farther downstream, the AW outflow from the Barents Sea, exiting through St. Anna Trough, joins the boundary current, but mostly subducts underneath the water originating from Fram Strait (Schauer et al., 2002). This is due to the strong air-sea-ice interaction in the Barents Sea, which cools and densifies the AW as it progresses across the sea. The two types of AW progressing eastward from here are referred to as the Fram Strait branch water (FSBW) and Barents Sea branch water (BSBW), respectively. Based on two years of mooring data from the Laptev Sea continental slope, the volume transport of AW (warmer than 0°C, within the category of FSBW) was calculated to be 3.1 ± 0.1 Sv (Pnyushkov et al., 2018). Upon reaching the Lomonosov Ridge, the boundary current bifurcates: part of the current progresses northward along the ridge, and the remaining part flows into the Canadian Basin along the continental margin (Rudels et al., 1999; Woodgate et al., 2007).

Direct velocity measurements of the AW boundary current in the western Arctic are rare. However, pathways of the water have been mapped out using water mass signatures, in particular the warm temperature core of the current and thermohaline intrusions associated with the AW (Li et al., 2020; McLaughlin et al., 2009; Swift et al., 1997; Woodgate et al., 2007). As such, a part of the boundary current is believed to get diverted into the interior along the Alpha-Mendeleev Ridge, and different branches are thought to progress through the complex topography of Chukchi Borderland. This includes a northern pathway around the perimeter of the Borderland—with a portion separating into the interior (McLaughlin et al., 2009; Smith

et al., 1999)—and an inner branch that flows along the continental slope. Recently it has been demonstrated that these two branches remain separated after emerging from the Borderland into the southern Canada Basin (Li et al., 2020; see Figure 1a). The inner branch is located between the 1,000–1,500 m isobaths, while the outer branch resides between the 2,500–3,000 m isobaths. Using nine repeat shipboard velocity sections occupied between 2003 and 2018, Li et al. (2020) estimated the mean volume flux of the combined flow to be 0.87 ± 0.13 Sv.

In addition to these AW branches on the mid and outer continental slope, a time dependent eastward flow of AW has been identified on the upper continental slope of the Beaufort Sea. Using data from a shelf-slope mooring array east of Pt. Barrow, AK, Pickart et al. (2011) revealed that, subsequent to an upwelling event, a narrow eastward-flowing jet of AW can form. This phenomenon has been named the "rebound jet", and it is located just seaward of the eastward-flowing shelfbreak jet of Pacific water that emanates from the Chukchi shelf (e.g., Lin et al., 2016; Nikolopoulos et al., 2009). The evolution of the shelfbreak jet and the rebound jet for a particularly strong upwelling storm was diagnosed using the mooring data in conjunction with a simplified model. During the storm, the flow on the outer-shelf and upper-slope is directed westward because of Ekman setup due to the easterly wind. After the cessation of the wind, the eastward-flowing shelfbreak jet of Pacific-origin water is re-established, while at the same time the AW in the rebound jet flows strongly to the east for a period of a few days before spinning down.

Pickart et al. (2011) diagnosed the dynamics of the rebound jet using their model. The jet arises because of the disparity in speeds between barotropic and baroclinic coastally trapped waves that are excited by the post-storm relaxation of the winds. Immediately after the winds die down, a fast-moving, eastward-propagating barotropic wave adjusts the sea surface height such that the surface velocity goes from strongly westward during the storm to near-zero after the storm. However, the isopycnals take more time to adjust because of the more slowly propagating baroclinic waves. As such, the isopycnals remain upward-tilted toward the shelf due to the previous upwelling, and the corresponding thermal wind results in a bottom-intensified flow of AW to the east. Using 6 years of data from the single shelf basin interaction (SBI) mooring near the shelfbreak of the Alaskan Beaufort Sea, at the same location of the mooring array used by Lin et al. (2019); Pickart et al. (2011), demonstrated that the post-storm occurrence of the rebound jet is ubiquitous. However, their study did not focus on the rebound jet, in part because their mooring was not well positioned to sample AW. Hence, there remain a host of questions regarding the jet, including its transport, cross-stream structure, and its relationship to the two offshore branches of AW.

In this study, we investigate the flow of AW on the continental slope of the Beaufort Sea using data from the full shelf-slope SBI mooring array deployed east of Pt. Barrow from 2002 to 2004. While Pickart et al. (2011, 2013) considered a single (strong) upwelling event, we use the full 2 year timeseries and focus on the AW component of the boundary current system. The paper is structured as follows. In Section 2 we describe the mooring array data along with the atmospheric reanalysis product used. In Section 3 the forcing, characteristics, and dynamics of the rebound jet are investigated. In Section 4 the mooring data are used to shed further light on the onshore branch of AW that resides over the mid continental slope, including how the flow is impacted by the wind field. Conclusions are presented in Section 5.

2. Data and Methods

2.1. Mooring Data

A mooring array was deployed over the Alaskan Beaufort shelfbreak and slope near 152°W from August 2002 to September 2004, as part of the SBI program (Figure 1b). Seven moorings (BS2-BS8) were situated onshore to offshore with ~5 km resolution, except for the offshore-most mooring BS8 which is ~10 km apart from BS7. This spacing is smaller than the internal Rossby radius of deformation in the western Arctic estimated using a vast hydrographic data set (Zhao et al., 2014). An eighth mooring, BS1, was located inshore of BS2, but since it did not function in year one and did not sample AW, it is not considered here. The array was located roughly 150 km to the east of Pt. Barrow. Hydrographic measurements were obtained using a coastal moored profiler (CMP) at moorings BS2-BS6, and a McLane moored profiler (MMP) at moorings BS7-8, which provided vertical traces of temperature and salinity extending from near the sea floor to nominally 40 m beneath the surface. The vertical resolution was 2 m, and profiles were obtained every 6 h

for the CMPs (0, 6, 12, 18 UTC) and twice daily (0 and 6 UTC) for the MMPs. MicroCATs, recording hourly, were deployed at the base of each mooring to provide calibration information for the CMPs. Details regarding the processing and accuracy of the CMP and MMP data are provided in Spall et al. (2008). Velocity was measured using upward-facing acoustic Doppler current profilers at the base of moorings BS2-BS6. These provided hourly profiles with a vertical resolution ranging from 5 m (BS2-3) to 10 m (BS4-6). At moorings BS7-8 an acoustic current meter (ACM) was attached to the MMP, providing two profiles of velocity per day with a vertical resolution of 2 m. Details concerning the velocity data, including the de-tiding, are provided by Nikolopoulos et al. (2009). Overall, the data return was excellent. However, there were some significant data gaps. Most notably, the CMP at BS6 did not function in year 2, and the ACM at BS8 failed after 8 months in year one. When comparing the mooring data to the atmospheric forcing in Section 4, we consider the same 8 months time period for the yearone winds to be consistent.

We constructed vertical sections of potential temperature and potential density (referenced to the sea surface), salinity (practical salinity scale), and along-stream velocity. Following Nikolopoulos et al. (2009), the along-stream direction is taken to be 125°T (where 0°T is northward and the angle increases clockwise), based on the orientation of the depth-mean flow and principle axis of variance. The gridding was done using Laplacian-Spline interpolation with a horizontal grid spacing of 0.5 km and a vertical grid spacing of 2 m (5 m) for the hydrography (velocity).

2.2. Wind Information

Two sources of wind data are used in the study. The 10 m wind timeseries from the meteorological station in Utqiaġvik, AK (formerly known as Barrow, AK) were obtained from the National Climate Data Center of the National Oceanic and Atmosphere Administration (http://www.ncdc.noaa.gov/). The data were subject to further quality control, which is explained in detail in Pickart et al. (2013). The temporal resolution of the record is 1 h, and we used the alongcoast component, which is 105°T. Previous studies have demonstrated that the winds at Utqiaġvik are similar to those in our study region (Nikolopoulos et al., 2009; Pickart et al., 2009). To provide a larger scale context of the atmospheric forcing, we use the 10 m winds from the ERA5 reanalysis product, obtained from https://www.ecmwf.int/en/forecasts/datasets/reanalysis-datasets/era5. ERA5 is the fifth–generation European Center for Medium-Range Weather Forecast atmospheric global reanalysis, with a horizontal grid spacing of 0.25° and temporal resolution of 1 h. The data were subsampled to 3 hourly resolution for our analysis.

2.3. Sea Surface Height Data

We use the monthly-averaged satellite sea surface dynamic topography and geostrophic velocity data-set described in Armitage et al. (2016), which spans the time period 2003–2014. In ice-covered regions the absolute dynamic topography is estimated from leads in the pack-ice, which is used together with the conventional open-ocean altimetry product to produce composite fields. The GOCO03s geoid (Mayer-Gurr et al., 2012) is used to compute absolute sea surface heights. The spatial resolution of the data is 0.25° and 0.75° in the meridional and zonal directions, respectively. The northern extent of the satellite coverage is 81.5°N.

3. Rebound Jet Events on the Continental Slope

Previous studies using the SBI mooring data have concentrated mainly on the Pacific Water component of the boundary current (e.g., Brugler et al., 2014; Lin et al., 2019; Nikolopoulos et al., 2009;). The two-year mean potential temperature and along-stream velocity sections are shown in Figure 2, reproduced from Li et al. (2020). The warm water in the vicinity of the shelfbreak is comprised of Pacific Summer Water, which is due to the presence of both Bering Summer Water and the very warm Alaskan Coastal Water. Below this is the layer of cold Pacific Winter Water (colder than −1.2°C), centered at 150 m. The temperature of this layer is moderated near the continental slope due to the common occurrence of wind-driven upwelling, which brings warm AW to the vicinity of the shelfbreak (Lin et al., 2019). Beneath the winter water is a thick layer of warm AW, with a temperature maximum near 400 m. The interface between the AW and the Pacific Water is the 27.06 kg m^{-3} isopycnal, which corresponds to the peak stratification at the base of the Pacific winter water layer (Nikolopoulos et al., 2009). Also marked in Figure 2a is the interface between the FSBAW

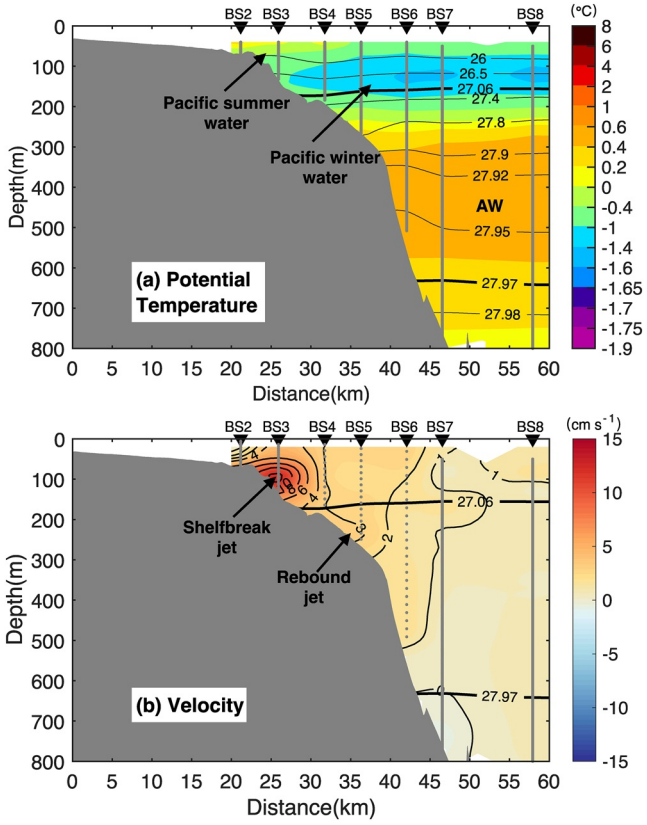

Figure 2. Two-year mean sections from the shelf basin interaction mooring array. (a) Potential temperature (color, °C) overlain by potential density (contours, kg m^{-3}). The gray dots show the data coverage (which are so close together that they appear as lines), and the symbols along the top denote the moorings. The bounding isopycnal (27.06 kg m^{-3}) between the Pacific Water and Atlantic Water (AW) is highlighted, as is the isopycnal (27.97 kg m^{-3}) separating the Fram Strait Branch AW and Barents Sea Branch AW. (b) Alongstream velocity (color and contours, cm s^{-1}), where positive is directed toward 125°T. The gray dots show the data coverage. The locations of the shelfbreak jet and the rebound jet are labeled. The bathymetry is from a shipboard echosounder.

and BSBAW (27.97 kg m^{-3}, Li et al. (2020)). The precise choice of this interface does not impact our analysis below. The AW is found primarily seaward of mooring BS3.

In the mean, there is a bottom-intensified shelfbreak jet which advects Pacific Water eastward. The volume transport of the jet varies interannually between 0.02–0.12 Sv (Brugler et al., 2014). Seaward of this and deeper in the water column is the signature of the rebound jet of AW, with an average speed >3 cm s^{-1} near 250 m depth. Instantaneously, however, it can exceed 50 cm s^{-1} (Pickart et al., 2011). As discussed in the introduction, the rebound jet is an intermittent feature that follows upwelling events (Lin et al., 2019), and its mean transport is only 0.05 Sv. Nonetheless, it appears in the 2 year mean section, and is likely what Aagaard (1984) referred to as the Beaufort undercurrent.

3.1. Identification and Statistics of Rebound Jet Events

The single rebound jet event that Pickart et al. (2011) discussed had the largest velocity signal at mooring BS5, appearing shortly after the cessation of the easterly wind. This is true of all the events over the 2 year record. Accordingly, we define two criteria that characterize a rebound jet event at the mooring array: (a) The near-bottom alongstream velocity anomaly at BS5, relative to the 2 year mean and averaged between 200–250 m, is greater than 0 cm/s and lasts more than one day. This means we are only considering rebound jet events where the velocity signal exceeds the long-term mean. (b) The mean alongcoast wind from t_1 to t_2 is easterly, where t_1 is three days prior to the event as defined by criterion (a), and t_2 is when the eastward alongstream velocity at BS5 peaks. There are a small number of events that are less than one day apart from the previous event or following event. In these instances, the two back-to-back events are considered as a single event. After applying criterion (a), 77 potential events were identified. Twenty of those corresponded to instances of westerly wind and were associated with downwelling events (which also have increased velocity in the lower layer) as reported by Foukal et al. (2019). The remaining 57 instances satisfy criterion (b) and hence are identified as rebound jet events.

The occurrences of the rebound jet over the 2 year time period of the mooring array are shown in Figure 3. The mean duration of an event is 3.2 ± 1.6 days (standard deviation), and the longest event is 8.5 days. Notably, every upwelling event identified by Lin et al. (2019) during the 2 year SBI period was associated with a subsequent rebound jet. However, there are a few instances identified here when a rebound jet does not follow one of the upwelling events identified by Lin et al. (2019), even though there was an easterly wind. This is likely because the criterion used by Lin et al. (2019) only identified relatively strong wind-driven upwelling events. As is the case for upwelling, rebound jet events thus occur in all months of the year, but are most frequent in the fall (Figure 3; Lin et al., 2019; Pickart et al., 2013). The duration of the rebound jets is smaller during the summer (2.2 ± 1.0 days) versus the other three seasons (3.6 ± 1.7 days).

3.2. Mean Depiction of the Rebound Jet

Inspection of the individual rebound jet events reveals that they all had the same general structure with a maximum velocity at mooring BS5. To quantify this structure, we constructed a composite vertical section from the 57 events (where the properties for each event were averaged from t_1 to t_2, then these mean sections were averaged together, Figure 4). This reveals that the typical rebound jet exceeds 15 cm s^{-1}, with its core located at mooring BS5 near the 250 m isobath (Figure 4b). The mean jet extends seaward roughly 20 km.

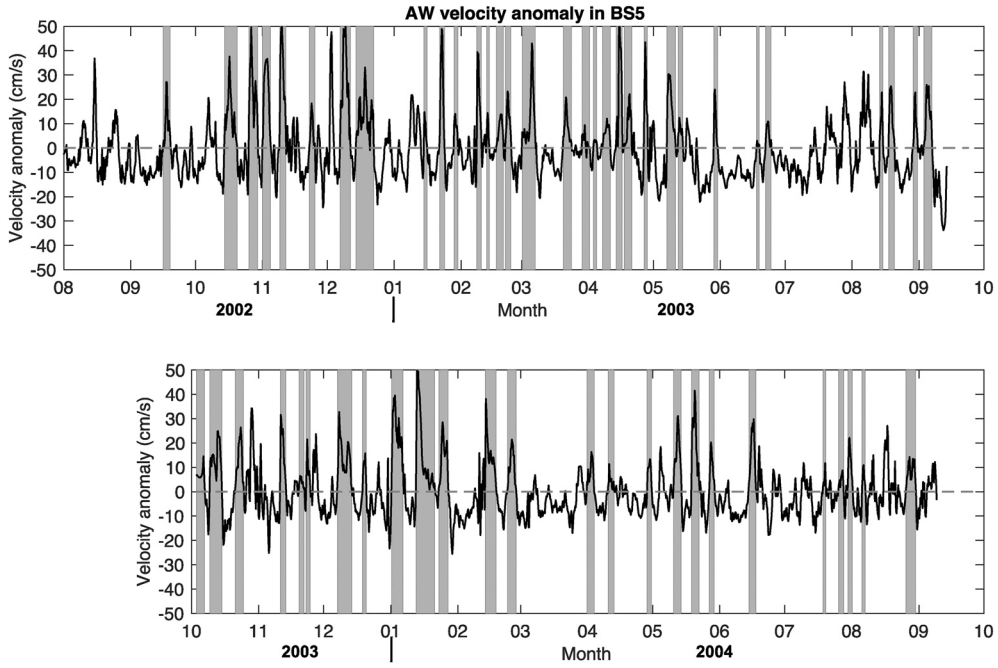

Figure 3. Rebound jet events (gray bars) during the time period of the shelf basin interaction mooring array. The black curve is the alongstream velocity anomaly averaged over the depth range 200–250 m at mooring BS5.

In addition to the appearance of the rebound jet, the shelfbreak jet becomes re-established following the upwelling and continues to flow eastward after the rebound jet subsides. In order to remove the signature of the emerging shelfbreak jet, we subtracted the mean velocity section (Figure 2b) from the rebound jet composite (Figure 4b), which isolates the structure of the temporary rebound jet (Figure 4c). This demonstrates that, while the response is greatest in the AW layer, the shallower Pacific Water is also accelerated as part of the rebound jet in the region from the shelfbreak extending out to mooring BS7. In contrast to the velocity, the hydrographic structure of the water column during a rebound jet event is similar to the mean state (compare Figures 4a and 2a).

Although the rebound jet influences the Pacific Water layer, the focus of this study is on the AW. As mentioned above, the 2 year mean AW transport of the jet is <0.05 Sv. This is an order of magnitude smaller than the combined transport of the two branches of AW located farther offshore, 0.87 ± 0.13 Sv (Li et al., 2020, where the uncertainty is the standard error). To compute the transport of the composite rebound jet event, we chose the domain below the 27.06 kg m^{-3} isopycnal (i.e., the AW) and seaward to mooring BS7 (although the rebound jet often extends to BS8, as discussed below). This gives a transport of 0.24 ± 0.01 Sv. For the strongest event the value is 0.58 Sv, which is comparable to the two offshore branches (the maximum synoptic value of the combined branches was 1.35 Sv Li et al., 2020).

3.3. Time Evolution of the Rebound Jet

To investigate the spin-up and spin-down of a rebound jet event, we created depth-time composites of different variables. This was done using normalized time, t_n, ranging from 0 at the beginning of the event to 1 at the end (see Lin et al. (2019) and Foukal et al. (2019) who used the same methodology for upwelling and downwelling events, respectively). We consider as well the time periods immediately prior to and subsequent to the event ($-0.5 \leq t_n \leq 1.25$).

Figure 5 shows the composite alongcoast wind and alongstream velocity at BS5. Before the event, the wind is easterly (negative) at 5 m s^{-1}, and decreases prior to the onset of the rebound jet to roughly 3.5 m s^{-1}. This period corresponds to the end of an upwelling event, which is evident in the velocity composite showing a surface-intensified westward flow characteristic of the reversed shelfbreak jet. Previous studies have shown

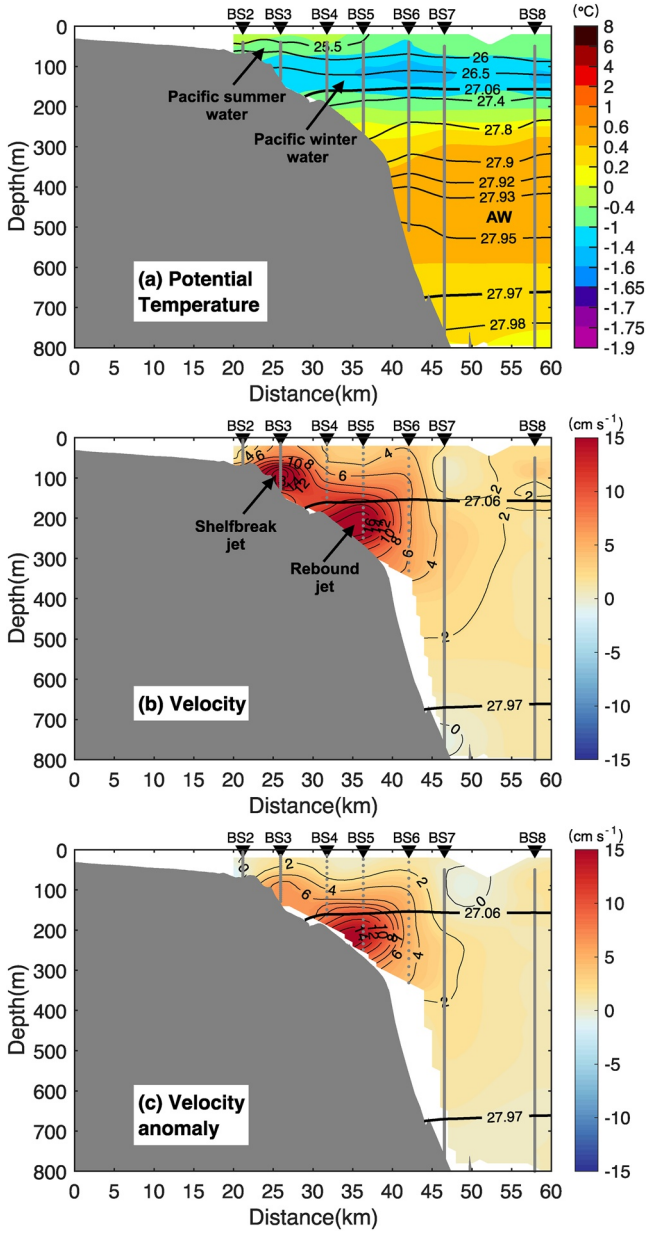

Figure 4. Composite vertical section of all 57 rebound jet events. (a) Potential temperature (color, °C) overlain by potential density (contours, kg m^{-3}). The gray dots show the data coverage, and the symbols along the top denote the moorings. The bounding isopycnal (27.06 kg m^{-3}) between the Pacific Water and Atlantic Water (AW) is highlighted, as is the isopycnal (27.97 kg m^{-3}) separating the Fram Strait Branch AW and Barents Sea Branch AW. (b) Alongstream velocity (color and contours, cm s^{-1}). The gray dots show the data coverage. The locations of the shelfbreak jet and the rebound jet are labeled. (c) Velocity anomaly of the rebound jet composite relative to the two-year mean.

that upwelling occurs when the easterly wind exceeds roughly 4 m s^{-1} (Pickart et al., 2013; Schulze & Pickart, 2012), which is consistent with the evolution in velocity from westward to eastward in Figure 5 as the easterly wind dies down. Lin et al. (2019) composited 115 upwelling events over 6 years and showed that the average peak alongcoast wind was 5.3 m s^{-1} from the east, suggesting that the beginning of our composite, $t_n = -0.5$, is close to the period of maximum upwelling. We note that the reversed flow in Lin et al. (2019) composite was significantly larger than that in Figure 5b (20 cm s^{-1} vs. 10.7 cm s^{-1}). This is because their composite was at mooring BS3 which maximizes the shelfbreak jet response, whereas ours is at mooring BS5 in the heart of the rebound jet (see Figure 4b). The spin-up of the rebound jet is fairly rapid (Figure 5b). As noted above, it is present throughout the water column, but the largest signal is in the AW layer, reaching 23 cm s^{-1} at its peak. The event is asymmetric in that the spin-down occurs more slowly than the spin-up.

The composites of the hydrographic fields at BS5 are shown in Figure 6. Prior to the development of the rebound jet, the water in the AW layer is warmer and saltier. This is water that has been upwelled from deeper in the basin due to the enhanced easterly winds. The reader should keep in mind that, as with the velocity, the largest upwelling response in hydrography also occurs onshore of mooring BS5. When the upwelling ends and the rebound jet appears, this warmer and saltier water returns to the basin. While the peak eastward velocity of the rebound jet occurs near $t_n = 0.35$, the properties of the AW in the rebound jet reach their coldest/freshest values near $t_n = 0.9$. Hence, as with upwelling, there is an offset in the peak kinematic and hydrographic response for the AW rebound jet. Interestingly, the Pacific Winter Water layer is colder during the rebound jet event. This is likely an advective signal from upstream (from the west), as the velocity signature of the jet extends into the Pacific Winter Water layer.

We constructed a similar set of alongstream velocity composites for all of the moorings (Figure 7). In line with the composite vertical section (Figure 4b), the largest velocity response was at moorings BS3 and BS5, although the former was mostly due to the re-establishment of the Pacific Water shelfbreak jet (Figure 4c). Seaward of the shelfbreak jet, there is a measurable signal of the rebound jet across the rest of the array. In terms of the anomaly from the start of the composite ($t_n = -0.5$, prior to the event), the average response during the rebound jet (t_n = 0-1) was 13.4 cm s^{-1} at mooring BS4, 18.7 cm s^{-1} at BS5, 5.7 cm s^{-1} at BS6, 2.4 cm s^{-1} at BS7, and 2.0 cm s^{-1} at BS8. Only 72% of the events had a measurable signature at the two offshore moorings (vs. 100% at the other moorings). In terms of depth, the rebound jet signature extended to the bottom (or more precisely to the deepest measurement depth) at all of the moorings.

3.4. Dynamics of the Rebound Jet

As discussed in the introduction, Pickart et al. (2011) explained that the rebound jet arises after an upwelling storm due to the fast adjustment of the sea surface height, via a barotropic wave, and the slower adjustment of the isopycnals, via baroclinic waves. This was diagnosed using a numerical simulation. We now seek to elucidate this using our observations. In particular, we seek to determine if stronger easterly winds lead to a stronger rebound jet. The idea is that stronger easterly winds

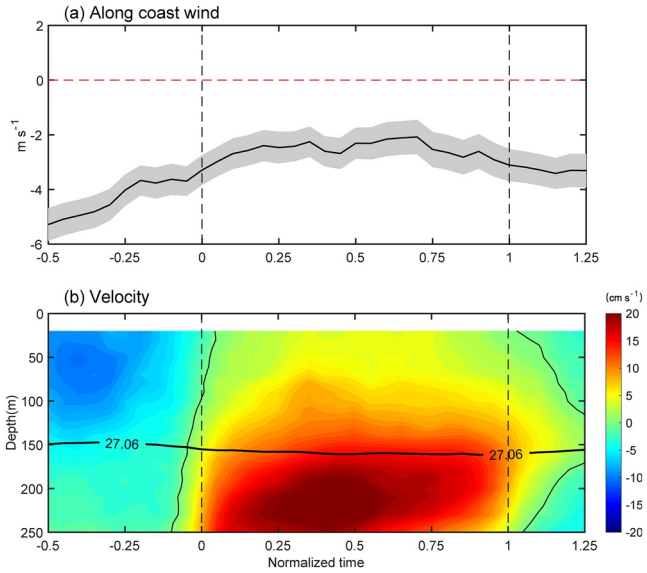

Figure 5. Composite rebound jet event, plotted as a function of normalized time. (a) Alongcoast wind speed (m s^{-1}; negative is easterly). The shading represents the standard error. (b) Alongstream velocity (cm s^{-1}) at mooring BS5. The 0 cm s^{-1} contour is indicated by the thin black line. The 27.06 kg m^{-3} isopycnal, separating the Pacific Water and AW, is highlighted by the thick black line.

should deflect the isopycnals upwards towards the shelf to a greater extent via upwelling. Then, after the sea surface relaxes, the enhanced isopycnal tilt should result in a stronger rebound jet via thermal wind.

To determine if this is the case, the first step is to determine if there is a relationship between wind and isopycnal tilt. Previous work has demonstrated that stronger easterly winds draw denser water to the vicinity of the shelfbreak (Lin et al., 2019). In particular, the bottom density anomaly at mooring BS3 is greater for more powerful storms. However, Lin et al. (2019) did not address isopycnal tilt. Here we estimate the tilt by the average change in depth of the isopycnals between mooring BS4 and BS7 (we could not use mooring BS6 for this calculation because it had no hydrographic measurements in year 2). For each of the 57 rebound jet events we constructed a timeseries of isopycnal displacement so defined, starting three days prior to the event to the time when the rebound jet was at its peak (this is the time period t_1 to t_2 used in Section 3.2 for identifying events). After removing outliers, we chose the maximum displacement as our metric (results were not sensitive to this choice).

The isopycnal displacement is regressed against the alongcoast wind stress in Figure 8a, where the wind stress is the maximum value during the same time period t_1 to t_2 (the maximum winds occur early in the period, since the rebound jet spins up as the winds abate). This reveals that stronger winds generally lead to a greater isopycnal displacement. Next, we compared the isopycnal displacement to the strength of the rebound jet, in particular the peak value of the jet at t_2. This also shows a statistically significant relationship, indicating that stronger isopycnal tilt is associated with a stronger rebound jet (Figure 8b). These results support the underlying dynamics of the rebound jet laid out by Pickart et al. (2011). Hence, we now know that stronger easterly winds not only lead to a stronger reversed shelfbreak jet and denser water upwelled from the basin (Lin et al., 2019), but they also result in a stronger rebound jet following the upwelling.

4. Atlantic Water Boundary Current Seaward of the Rebound Jet

Li et al. (2020) demonstrated that there are two branches of FSBAW, seaward of the rebound jet, that flow beneath and counter to the Beaufort Gyre – referred to as the onshore branch and the offshore branch, respectively. Using nine repeat shipboard hydrographic/velocity sections over a span of 15 years, they showed that the onshore branch was situated between the 1,000 and 1,500 m isobaths, and the offshore branch ranged between the 2,500 and 3,000 m isobaths. Since mooring BS8 was located at 1,400 m, one wonders if the onshore branch was detected by the mooring. Li et al. (2020) also investigated the variability of the two AW branches and suggested a relationship between the strength of the wind stress curl over the Canada Basin and the volume transport of the branches. This is perhaps not surprising since the eastward flow of AW is directly beneath the Beaufort Gyre, and the gyre strength is largely controlled by the wind stress curl (Regan et al., 2019). This is in line with the model result of Karcher et al. (2007) who suggested that the cyclonic AW circulation can be modulated by the Beaufort Gyre via atmospheric forcing. It is consistent as well with the idealized model results of Lique and Johnson (2015). With only nine realizations, however, Li et al. (2020) were not able to obtain statistically significant results regarding the connection between the wind forcing and the strength of AW boundary current branches. If mooring BS8 captures part of the onshore AW branch, it would provide an opportunity to test this relationship more robustly.

4.1. Comparison Between 2002–2003 and 2003-2004

As it happens, the signature of the Fram Strait Branch AW (hereafter referred to simply as AW) at mooring BS8 was different in the two SBI mooring years. This is demonstrated in Figure 9, which shows the mean hydrographic and velocity sections for each year (Note that the BS8 year 1 deployment is from August 2002

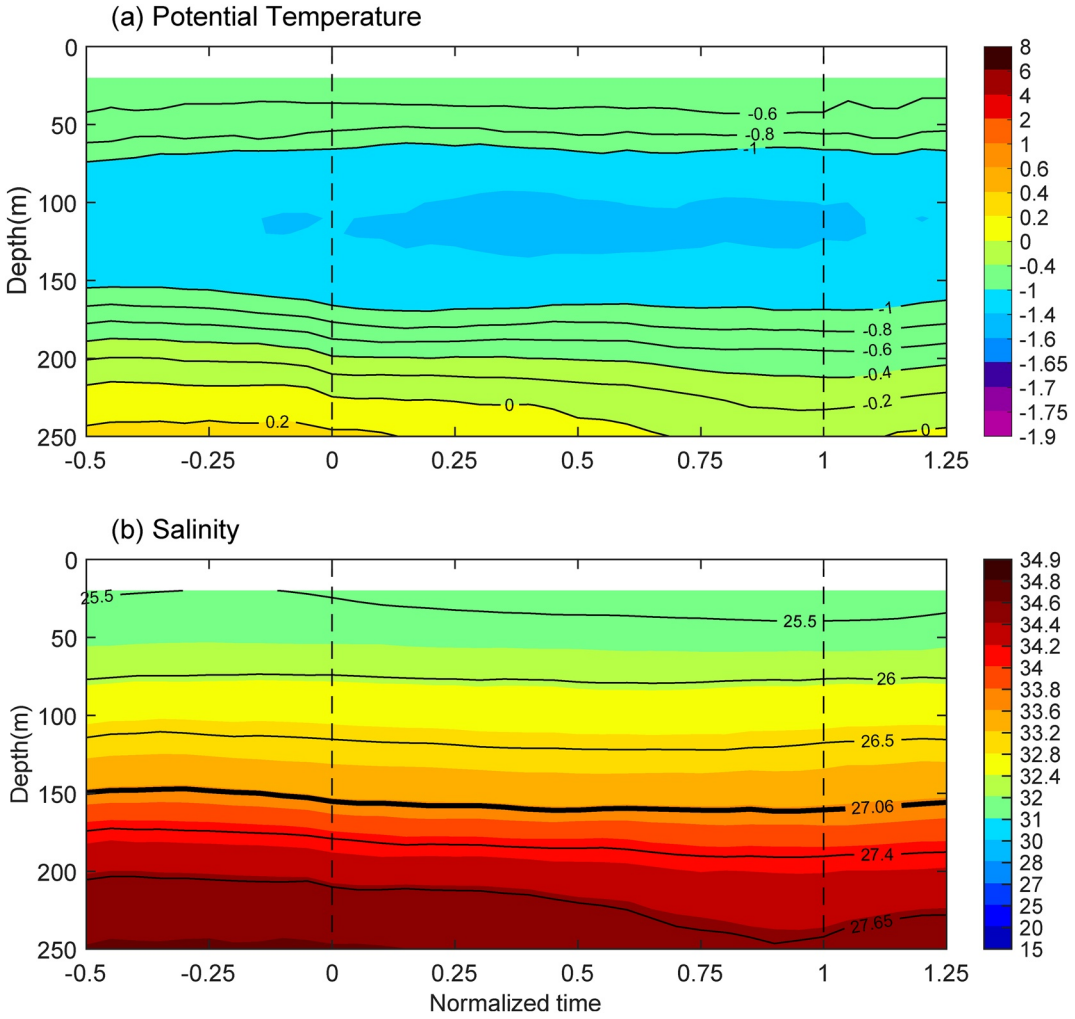

Figure 6. Composite rebound jet event hydrographic fields at BS5, plotted as a function of normalized time. (a) Potential Temperature (°C, color and contours). (b) Salinity (color) overlain by potential density (contours, kg m^{-3}). The 27.06 kg m^{-3} isopycnal, separating the Pacific Water and Atlantic Water, is highlighted by the thick black line.

to March 2003, and the year 2 deployment is from October 2003 to September 2004.) While the signature of the shelfbreak jet and rebound jet are similar in both years, the flow at mooring BS8 was predominantly westward in year 1 versus eastward in year 2 (Figures 9c and 9d). This is evident in the depth-averaged (200–700 m) AW flow (Figure 10):In year 1 the depth-averaged velocity was directed to the northwest and not significantly different than zero, while in year 2 it was directed eastward at 1.7 ± 0.6 cm s^{-1}. This is comparable to the mean speed of the onshore AW branch computed by Li et al. (2020) using shipboard data (1.2 ± 1.0 cm s^{-1}) as well as the magnitude of the flow of AW entering the Canadian Basin east of the Lomonosov Ridge (2 cm s^{-1}; Woodgate et al., 2001). The conclusion is that, in year 2, mooring BS8 predominantly measured the onshore AW branch, while in year 1 this was not the case. This is supported by the corresponding temperature sections (Figures 9a and 9b). Li et al. (2020) demonstrated that the two AW branches are associated with warm temperature cores as well. In Figure 9 we have included the bounding isotherm (0.55°C) used by Li et al. (2020) to identify the warmest part of the AW layer. One sees that this temperature core is more pronounced in year 2 (even extending to mooring BS7).

As shown by the depth-time composites in Section 3.3, the signature of the rebound jet extends offshore all the way to mooring BS8 (although the magnitude of the response is weak there). The enhanced eastward flow associated with downwelling events is also measured far seaward of the shelfbreak (Foukal et al., 2019). Together, upwelling and downwelling accounted for almost 50% of the record during the 2 year SBI period

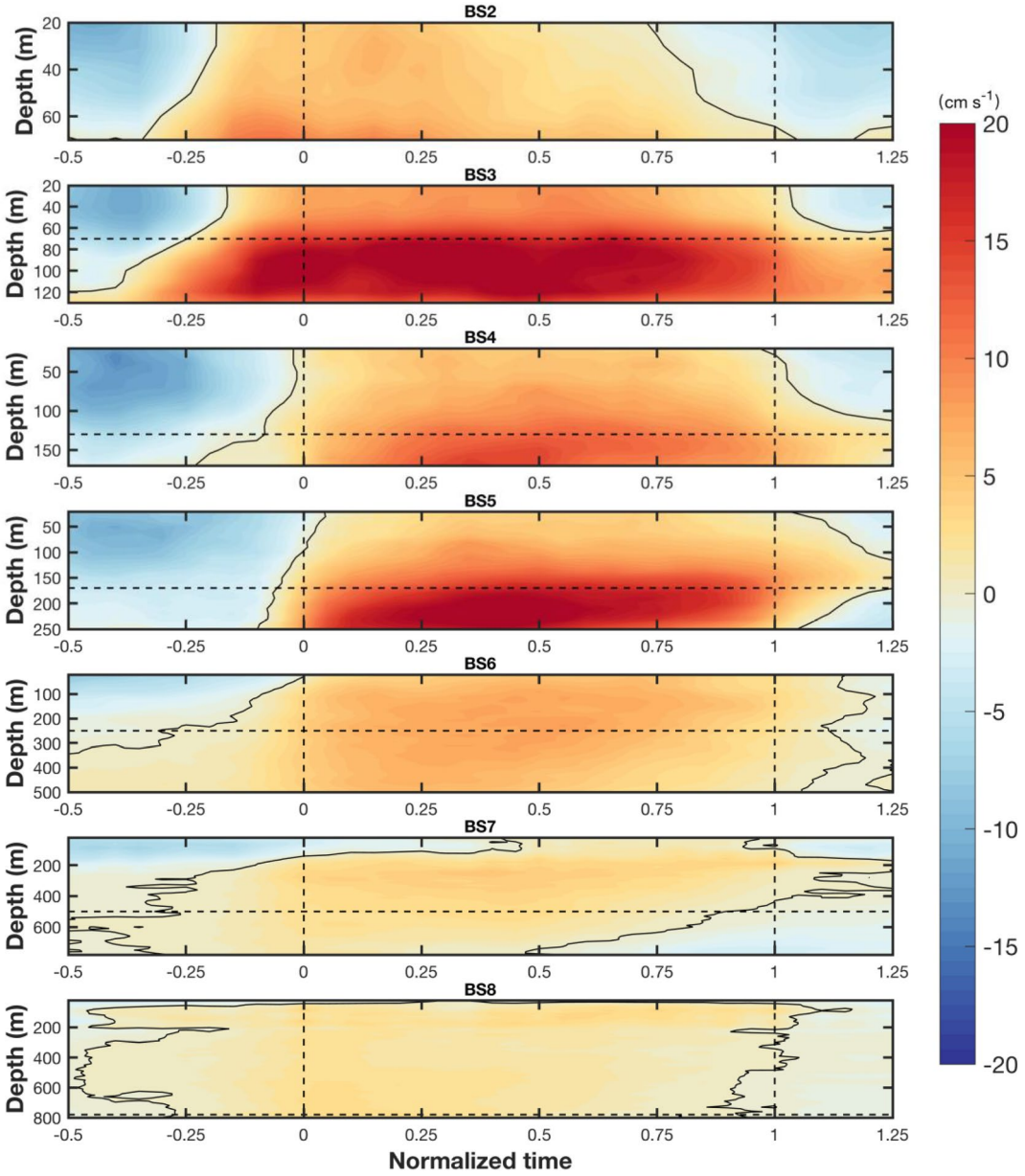

Figure 7. Composites of alongstream velocity (cm s^{-1}) of the rebound jet event, plotted as a function of normalized time, for moorings BS2-BS8. The 0 cm s^{-1} contour is indicated by the black line. The horizonal dashed line in each panel (except for the first one) represents the lower depth of the previous panel.

(Foukal et al., 2019). As such, one might expect to see a correlation in the alongstream flow across the array. In Figure 11 we have regressed the depth-averaged AW flow at mooring BS5 with that at BS8 for each of the years (the data were subsampled or interpolated into 6 h timeseries). In year 1 there is a clear relationship between the two, while in year 2 there is not. In particular, while the depth-averaged flow tends to co-vary at the two sites in the first year, with different amplitudes, the flow at BS8 in year two is more consistently to the east irregardless of the flow at BS5. This is another indication that BS8 is influenced by the AW boundary current in the second year.

To shed further light on this, we consider different timescales. Recall that the mean duration of the rebound jet is 3.2 ± 1.6 days. Downwelling events also last this long on average (3.25 ± 1.8 days, Foukal et al., 2019). As such, we applied a 15-days high-pass filter to the velocity records in order to isolate the high frequency signal. Not surprisingly, this revealed a significant correlation between BS5 and BS8 for year 1 (r = 0.49,

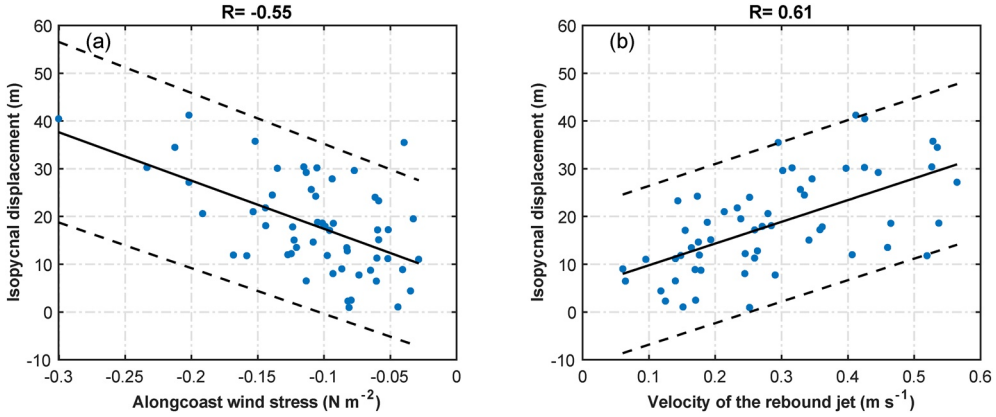

Figure 8. (a) Horizontal displacement of isopycnals (m) versus alongcoast wind stress (N m^{-2}, negative is easterly) for the rebound jet events (see text for details). (b) Horizontal displacement of isopycnals (m) versus maximum velocity of the rebound jet. The best fit lines (solid black) and 95% confidence levels (dashed black) are shown.

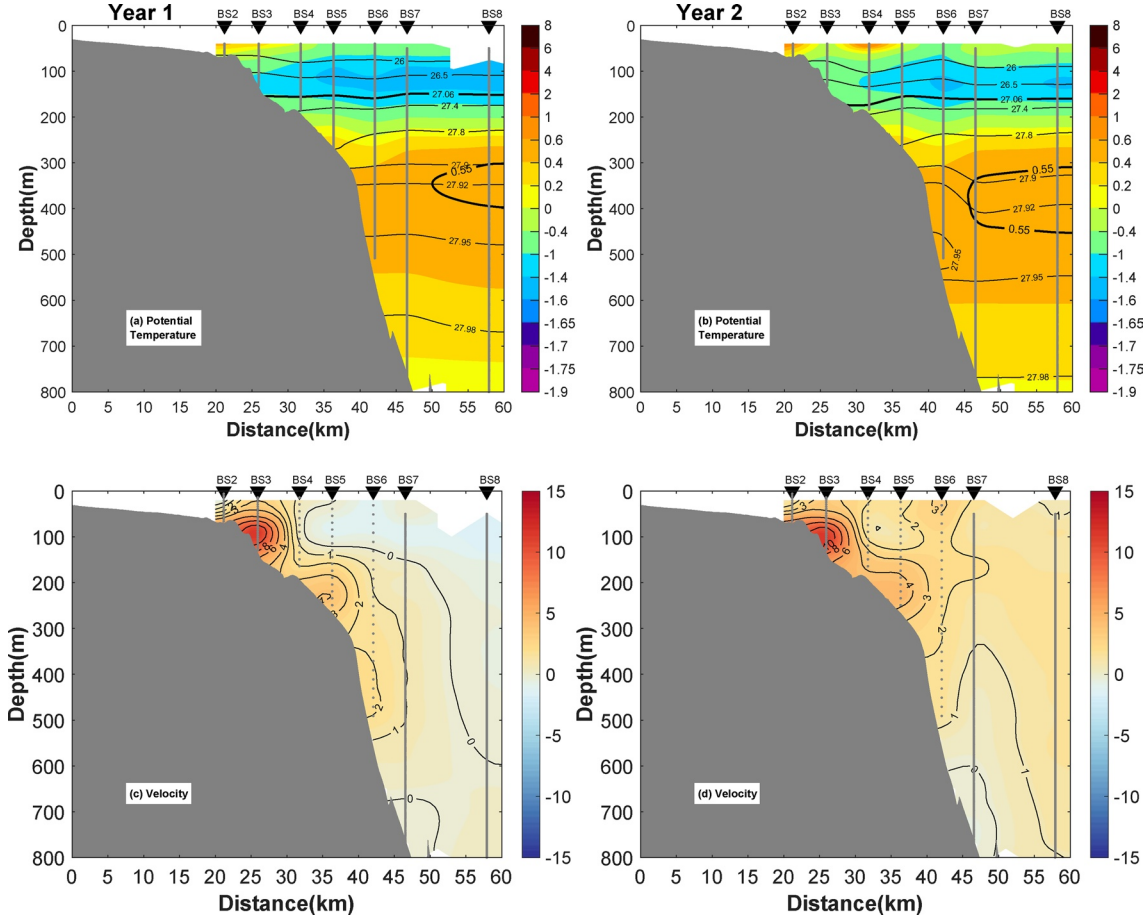

Figure 9. Mean vertical sections from the shelf basin interaction mooring array in the two deployment years. (a) Potential temperature (color,°C) overlain by potential density (contours, kg m^{-3}) in the first year. The 0.55°C temperature contour is highlighted by the thick black line. (b) Potential temperature in the second year. (c) Alongstream velocity (color and contours, cm s^{-1}) in the first year, where positive is directed toward 125°T. (d) Alongstream velocity in the second year. The other information is the same as in Figure 2.

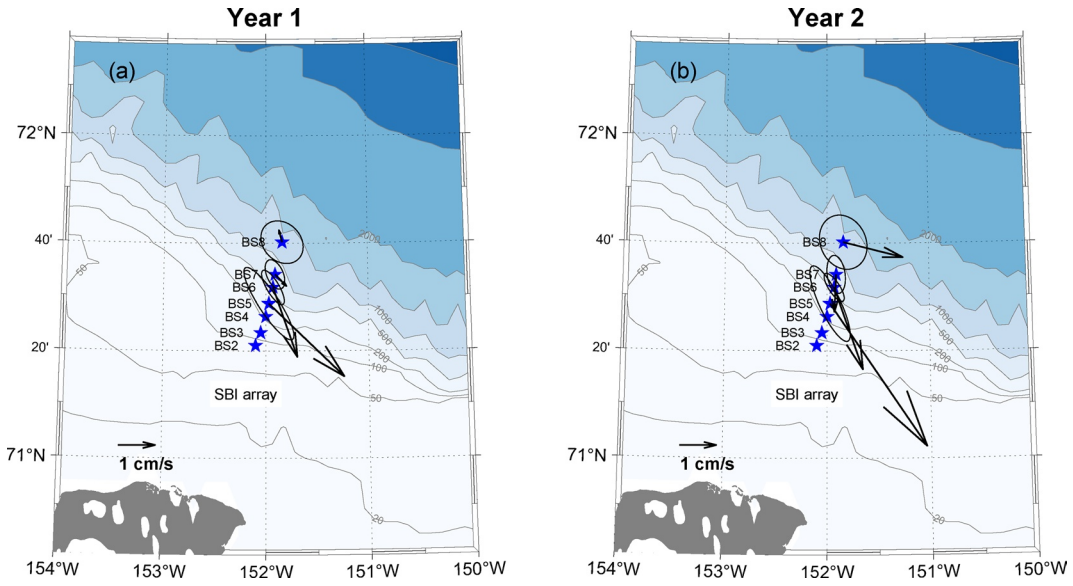

Figure 10. Depth–averaged velocity vectors in the Atlantic Water layer with standard error ellipses, in (a) the first year (2002–2003), and (b) the second year (2003–2004) of the shelf basin interaction mooring array.

$p < 0.05$), in line with Figures 11a (the comparison in Figures 11a takes into account all time scales). However, there is also significant correlation in this frequency range for year 2 ($r = 0.29$, $p < 0.05$). Hence, the high-frequency signal of rebound jets and downwelling events are measured for both deployment years at BS8. This implies that the AW boundary current signature at BS8 in year 2 (Figures 9d and 11b) varies on longer timescales.

To investigate this, we low-passed the BS8 alongstream velocity record using a 15 days filter. As mentioned above, Li et al. (2020) found a relationship between the transport of both branches of the AW boundary current and the wind stress curl averaged over the Canada Basin. In particular, they found that the transport varied in accordance with the time-mean wind stress curl averaged over the month preceding the shipboard section. We therefore computed the wind stress curl in the study region using the ERA5 reanalysis data, and subsequently low-passed this with the same filter width. We then computed the lagged correlation between the depth-averaged AW flow at BS8 and the wind stress curl at each data point in the domain. This was done separately for each year.

In year 2 there was significant correlation over the central part of the Canada Basin when the velocity lagged the wind stress curl, with peak correlation occurring at a lag of 19 days (Figure 12b). The sign of the correlation in year two is such that less negative wind stress curl results in enhanced eastward flow of the AW, also in agreement with Li et al. (2020). By contrast, there was weak correlation everywhere in year 1 at lags close to 19 days (Figure 12a). The only significant correlation for year 1 occurred at a short lag of 5 days, and the location of correlation was far to the north, outside of the Canada Basin (there is a hint of this in Figure 12a). These results demonstrate that both the alongcoast wind stress and the interior wind stress curl can influence the flow of AW at the seaward end of the SBI array. In year 1, when there was no signature of the AW boundary current, the effect of the local wind stress dominates. In year 2, when BS8 detected the onshore branch of the boundary current, this is only true at short time scales associated with rebound jets and downwelling events. At longer timescales the wind stress curl in the interior basin is the dominant factor.

4.2. Role of the Beaufort Gyre

We have demonstrated that the onshore branch of the AW boundary current was measured by mooring BS8 in 2003–2004, but not in 2002–2003. We now investigate the reason for this. Figure 13 shows the average wind stress curl in the study region for year 1 versus year 2. In the first year, the minimum wind stress curl was in the center of the basin, while in the second year the minimum was displaced southward adjacent

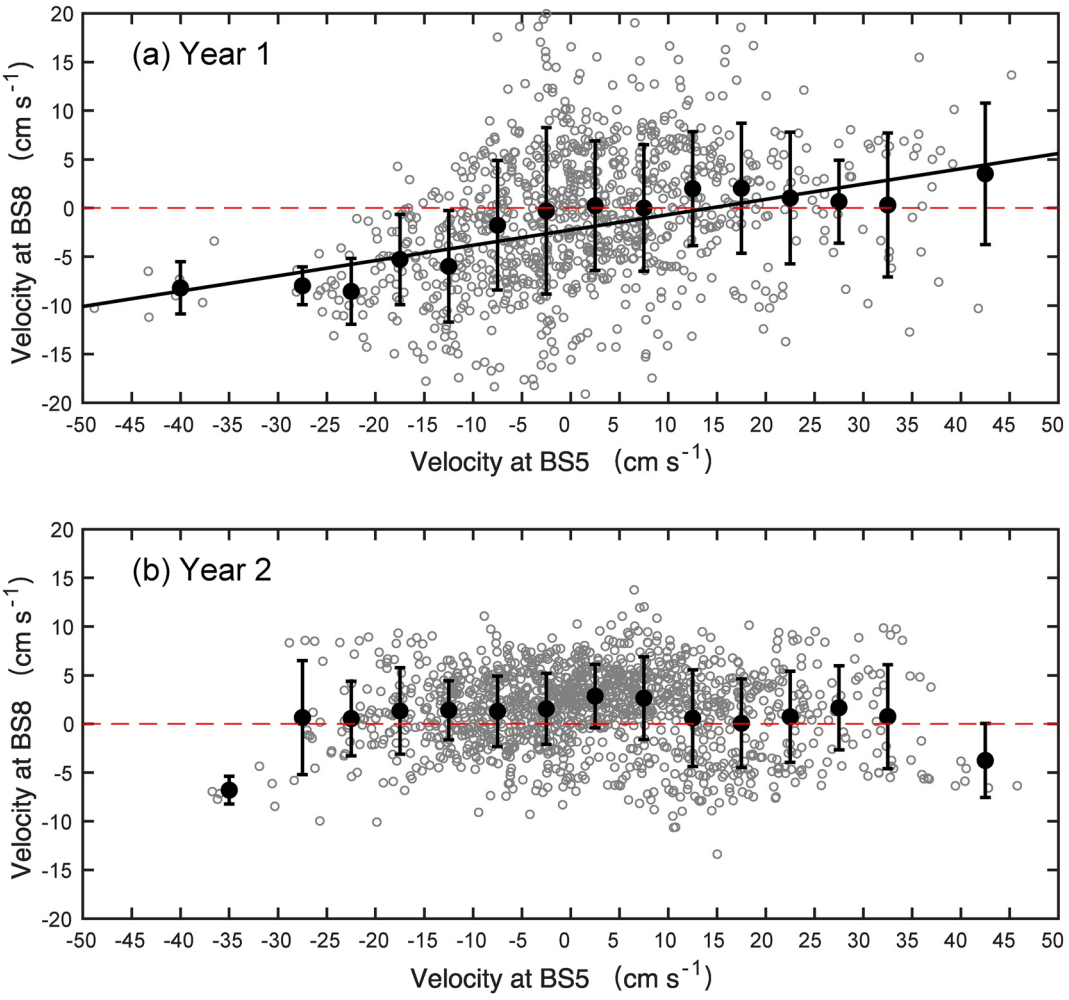

Figure 11. Depth–averaged velocity in the Atlantic Water layer (gray dots) at BS5 versus BS8 for (a) the first mooring year (2002–2003), and (b) the second mooring year (2003–2004). The black dots are the mean value of all points in each velocity interval (the intervals are larger at the two ends of the plot). The error bars are the standard deviation. The line of best fit of the interval means (solid black line) is plotted for year 1.

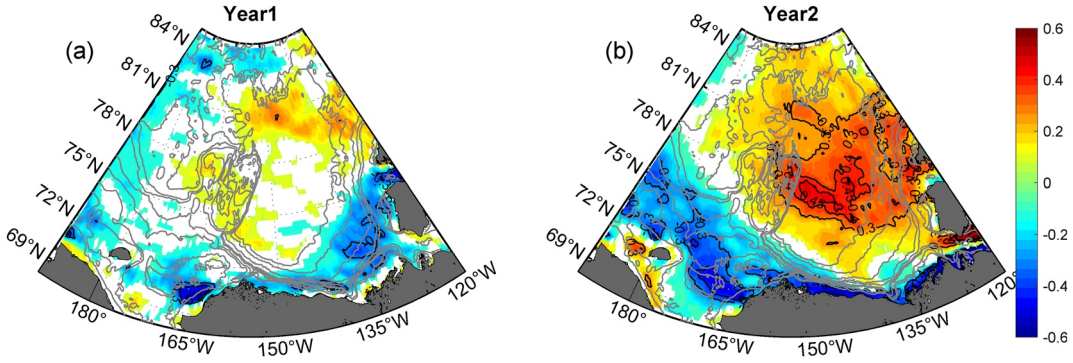

Figure 12. Map of the correlation coefficient between the 15 days low-passed, depth-mean AW velocity at BS8 and the 15 days low-passed wind stress curl at each grid point, where the velocity has been lagged by 19 days. (a) The first year (2002–2003), and (b) the second year (2003–2004) of the shelf basin interaction mooring array.

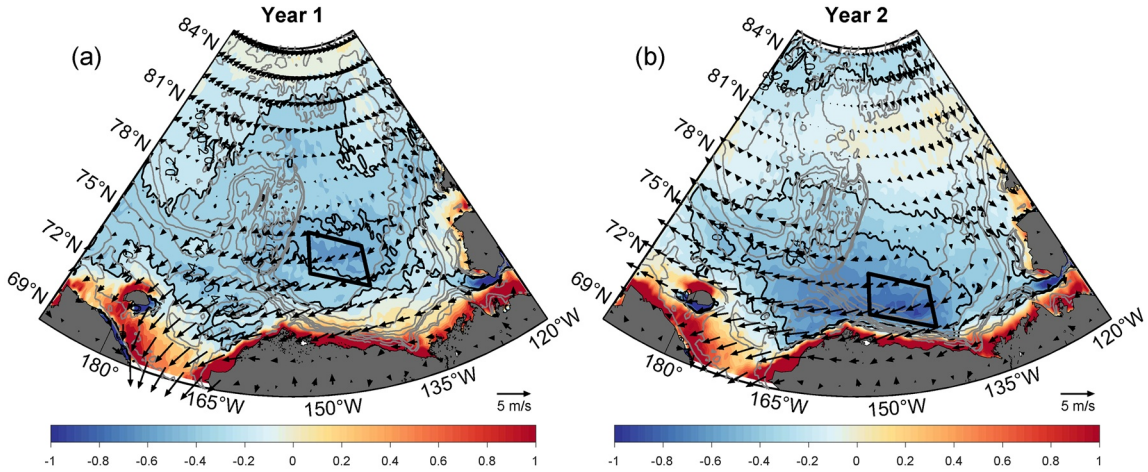

Figure 13. Mean wind stress curl (10^{-6} N m^{-3}, color) and 10 m wind vectors from ERA5 for (a) the first year (2002–2003), and (b) the second year (2003–2004) of the shelf basin interaction mooring array. The black box denotes the region of strongest negative wind stress curl in each year (used in the subsequent analysis).

to the continental slope, and was also larger in magnitude (more negative). What effect does this have on the Beaufort Gyre? To answer this, we delve further into the wind stress curl fields and also consider the satellite-derived, gridded sea surface geostrophic velocity product of Armitage et al. (2016). This product is available for the time period 2003–2014, which unfortunately means we can't compare the conditions in year 1 versus year 2 for surface geostrophic velocity.

We defined two boxes corresponding to the regions of minimum wind stress curl in year 1 and 2, respectively (Figure 13). We then computed a monthly timeseries of average wind stress curl for each box over the time period 2003 to 2014. The long-term mean value of wind stress curl in each box is comparable, approximately -0.27×10^{-6} N m^{-3}. We then identified the months when the monthly-mean value in the northern box was less than the long-term mean, while at the same time the monthly-mean value in the southern box was greater than the long-term mean. This was meant to identify instances when the pattern of wind stress curl was similar to year 1 (Figure 13a). The opposite was done to identify times when the wind stress curl pattern was similar to year 2 (Figure 13b). We further sorted the realizations in these two states into instances where the wind stress curl is less than or greater than the mean of the given state. The number of realizations (monthly means) in each of these four scenarios ranges from 8 to 11.

To assess the effect of these different wind stress curl scenarios on the Beaufort Gyre, we created corresponding composite maps of sea surface geostrophic velocity. The composites are shown in Figures 14a–14e. They reveal that, whether the wind stress curl minimum is located in the interior basin or near the southern boundary, when it is strong (more negative), the westward surface flow adjacent to the Beaufort slope is enhanced (Figures 14c and 14f). The effect of the change in the location of the wind stress curl minimum can be seen by considering the top two rows of Figure 14. Irregardless of the strength of the minimum, when it shifts southward the westward surface flow along the Chukchi slope and western portion of the Beaufort slope strengthens, while the westward flow along the eastern Beaufort slope weakens (Figures 14g and 14h).

The dividing line between these two regimes is where the SBI array is located (with some uncertainty due to the resolution of the satellite product). Since we are unable to compute a surface velocity composite for year 1, we created two climatological mean wind stress curl fields quantitatively similar to those in Figures 13a and 13b using the data from 2003–14, and constructed the associated surface velocity composites. The difference between these two velocity composites also shows the same pattern as in Figures 14g and 14h. Based on this, it is tempting to conclude that the SBI array was located to the left of the dividing line for year 1 minus year 2, meaning a stronger southern-arm of the Beaufort Gyre in year 1 at the longitude of the array.

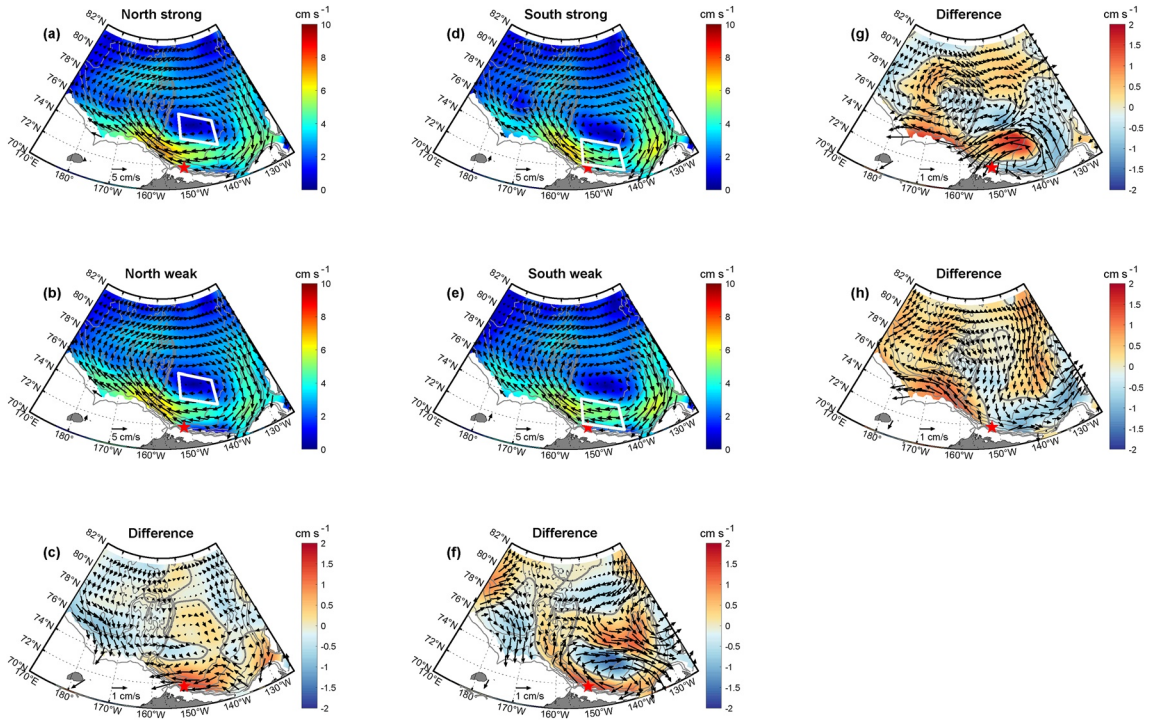

Figure 14. Composite fields of surface geostrophic velocity corresponding to the four wind stress curl scenarios described in the text, and their anomalies. (a) Strong and (b) weak negative wind stress curl in the central Canada Basin (within the white box). In each case the curl was stronger in the northern white box than in the southern white box. (c) The difference between (a) and (b). (d) Strong and (e) weak negative wind stress curl in the vicinity of the continental slope (within the white box). In each case the curl was stronger in the southern white box than in the northern white box. (f) The difference between (d) and (e). (g) The difference between (a) and (d). (h) The difference between (b) and (e).

In reality, the strength of the Beaufort Gyre relies on a combination of the wind stress curl and ice-ocean stress curl (Meneghello et al., 2018). However, to compute the latter one needs to know the surface velocity, which again we don't have for year 1. Interestingly, the ice concentration during the cold months of the year in the Canada Basin was on average 10% less in year 1 versus year 2. This implies that the ice keels would have been more mobile in the first year, which favors a larger ice-ocean stress (Martin et al., 2014; Pickart et al., 2013), and hence a stronger Beaufort Gyre. At this point it is unclear what the relative roles of wind and ice were in causing the westward flow measured at mooring BS8 in year 1, and hence the lack of a signature of the onshore AW branch. The underlying dynamics of the interaction between the Beaufort Gyre and AW boundary current need to be further explored, which is a topic for future study.

5. Conclusions and Discussion

In this study we have used two years of data from the shelf/slope SBI mooring array in the Alaskan Beaufort Sea, from 2002–4, to investigate aspects of the AW rebound jet—a ubiquitous feature that occurs after wind-driven upwelling events. Over the course of the 2 year period there were 57 such events. By constructing a composite event we revealed that on average they last 3.2 ± 1.6 days and transport 0.24 ± 0.01 Sv of AW. The rebound jet spins up quickly after the cessation of the easterly wind, with a peak velocity of 23 cm s^{-1}, then takes longer to spin down. During the event the isopycnals continue to slump from their upwelled state. The eastward velocity signature of the bottom-intensified jet is largest near the 250 m isobath, but extends well offshore of the shelfbreak. The seasonality of the rebound jet follows that of upwelling; hence they are most common in the fall. They occur often enough that the signature of the jet appears in the two-year mean velocity section.

Our observations also support the dynamical explanation put forth by previous modeling for the existence of the jet. The idea is that the slower baroclinic adjustment of the water column, following the decrease in wind speed, results in a thermal wind signature associated with enhanced eastward flow at depth. We

demonstrated that stronger easterly winds result in a more pronounced isopycnal tilt during upwelling events. This in turn was shown to be correlated with faster rebound jet velocities following the event. While this influences the Pacific Water layer as well, the response is greatest in the AW layer. In addition to the short-lived rebound jet, the eastward flow of the shelfbreak jet becomes re-established following the upwelling, which dominates the velocity response near the shelfbreak.

Seaward of the rebound jet, the offshore-most mooring of the array measured the onshore branch of the AW boundary flowing eastward in the Canada Basin. However, this was only evident in the second year of the mooring timeseries. We suspect that this is due to the influence of the Beaufort Gyre. In year 1, the negative wind stress curl that helps drive the gyre was largest in the central part of the Canada Basin, while in year 2 it was shifted southward toward the continental slope. Based on satellite-derived surface geostrophic velocity data, the former state corresponds to stronger westward flow along the continental slope in the Chukchi Sea and in the western Beaufort Sea close to the array. We surmise that this enhanced westward flow opposed the onshore branch of the AW boundary current which would otherwise be present at the offshore-most mooring, such that the two flows essentially canceled out each other at depth. Consequently, it would be difficult to detect a signal of the gyre or the boundary current. This can explain why the signature of rebound jet events/downwelling events was evident at the offshore-most mooring in year 1, and why there was no correlation of the flow at that site with the time-varying wind stress curl in the basin in year 1.

By contrast, in year 2 when the westward flow of the gyre was reduced near the array, the AW boundary current signal was more pronounced which overwhelmed the signature of rebound jet events/downwelling events (except at high frequency). In this scenario the AW boundary current is situated immediately adjacent to the southern arm of the Beaufort Gyre, and thus appears to be impacted by the wind stress curl forcing that drives variations in the gyre, with roughly a three-week lag. These results suggest a coupling of the dynamics associated with the Beaufort Gyre and the AW boundary current, which requires further investigation.

Our study has provided a better understanding of different aspects the AW boundary current system in the Beaufort Sea, and how it relates to wind forcing. As upwelling-favorable storms have become stronger and more frequent in recent years (Pickart et al., 2013), this implies that rebound jet events have also intensified and occurred more often. Further work is required to determine what the ecosystem ramifications are associated with this energized component of the AW boundary current system. It is also of interest to determine the longitudinal extent of the rebound jets, and if they affect the AW outflow through Fram Strait into the Nordic Seas.

Data Availability Statement

The mooring data used in the study can be found at http://www.eol.ucar.edu/projects/sbi/all_data.shtml.

Acknowledgments
Support for this research was provided by the National Science Foundation, under grants PLR-1504333 and OPP-1733564; the National Oceanic and Atmospheric Administration, under grant NA14OAR4320158; and the National Key R&D Program of China (2019YFA0606702).

References

Aagaard, K. (1984). The Beaufort undercurrent. In P. W. Barnes, D. M. Schell, & E. Reimnitz (Eds.), The Alaskan Beaufort Sea (47–71). Academic. https://doi.org/10.1016/b978-0-12-079030-2.50009-5

Aksenov, Y., Ivanov, V. V., Nurser, A. G., Bacon, S., Polyakov, I. V., Coward, A. C., et al. (2011). The Arctic circumpolar boundary current. *Journal of Geophysical Research*, *116*, C09017. https://doi.org/10.1029/2010JC006637

Armitage, T. W., Bacon, S., Ridout, A. L., Thomas, S. F., Aksenov, Y., & Wingham, D. J. (2016). Arctic sea surface height variability and change from satellite radar altimetry and GRACE, 2003–2014. *Journal of Geophysical Research: Oceans*, *121*, 4303–4322. https://doi.org/10.1002/2015JC011579

Brugler, E. T., Pickart, R. S., Moore, G. W. K., Roberts, S., Weingartner, T. J., & Statscewich, H. (2014). Seasonal to interannual variability of the Pacific water boundary current in the Beaufort Sea. *Progress in Oceanography*, *127*, 1–20. https://doi.org/10.1016/j.pocean.2014.05.002

Cokelet, E. D., Tervalon, N., & Bellingham, J. G. (2008). Hydrography of the West Spitsbergen current, Svalbard Branch: Autumn 2001. *Journal of Geophysical Research*, *113*, C01006. https://doi.org/10.1029/2007JC004150

Foukal, N. P., Pickart, R. S., Moore, G. W. K., & Lin, P. (2019). Shelfbreak downwelling in the Alaskan Beaufort Sea. *Journal of Geophysical Research: Oceans*, *124*, 7201–7225. https://doi.org/10.1029/2019JC015520

Karcher, M., F. Kauker, R. Gerdes, E. Hunke, and J. Zhang (2007). On the dynamics of Atlantic Water circulation in the Arctic Ocean, *Journal of Geophysical Research*, *112*, C04S02. https://doi.org/10.1029/2006JC003630

Koenig, Z., Provost, C., Sennéchael, N., Garric, G., & Gascard, J. C. (2017). The Yermak Pass branch: A major pathway for the Atlantic water north of Svalbard. *Journal of Geophysical Research: Oceans*, *122*, 9332–9349. https://doi.org/10.1002/2017JC013271

Kolas, E., & Fer, I. (2018). Hydrography, transport and mixing of the West Spitsbergen current: The Svalbard Branch in summer 2015. *Ocean Science*, *14*, 1603–1618. ocean-sci-discuss.net. https://doi.org/10.5194/os-14-1603-2018

Ladd, C., Mordy, C. W., Salo, S. A., & Stabeno, P. J. (2016). Winter water properties and the Chukchi polynya. *Journal of Geophysical Research: Oceans*, *121*, 5516–5534. https://doi.org/10.1002/2016JC011918

Li, J., Pickart, R. S., Lin, P., Bahr, F., Arrigo, K. R., Juranek, L., & Yang, X. Y. (2020). The Atlantic Water boundary current in the Chukchi borderland and southern Canada Basin. *Journal of Geophysical Research: Oceans*, *125*(8). https://doi.org/10.1029/2020JC016197

Lin, P., Pickart, R. S., Moore, G., Spall, M. A., & Hu, J. (2019). Characteristics and dynamics of wind-driven upwelling in the Alaskan Beaufort Sea based on six years of mooring data. *Deep Sea Research Part II: Topical Studies in Oceanography*, *162*, 79–92. https://doi.org/10.1016/j.dsr2.2018.01.002

Lin, P., Pickart, R. S., Stafford, K. M., Moore, G., Torres, D. J., Bahr, F., & Hu, J. (2016). Seasonal variation of the Beaufort shelfbreak jet and its relationship to Arctic cetacean occurrence. *Journal of Geophysical Research: Oceans*, *121*, 8434–8454. https://doi.org/10.1002/2016jc011890

Lique, C., & Johnson, H. L. (2015). Is there any imprint of the wind variability on the Atlantic Water circulation within the Arctic Basin? *Geophysical Research Letters*, *42*, 9880–9888. https://doi.org/10.1002/2015GL066141

Martin, T., M. Steele, & J. Zhang (2014). Seasonality and long-term trend of Arctic Ocean surface stress in a model, *Journal of Geophysical Research: Oceans*, *119*(3), 1723-1738.

Mauritzen, C. (1996). Production of dense overflow waters feeding the North Atlantic across the Greenland-Scotland Ridge. Part 1: Evidence for a revised circulation scheme. *Deep Sea Research Part I: Oceanographic Research Papers*, *43*(6), 769–806. https://doi.org/10.1016/0967-0637(96)00037-4

Mayer-Gurr, T., Savcenko, R., Bosch, W., Daras, I., Flechtner, F., & Dahle, C, C. (2012). Ocean tides from satellite altimetry and GRACE. *Journal of Geodynamics*, *59*, 28–38. https://doi.org/10.1016/j.jog.2011.10.009

McLaughlin, F. A., Carmack, E. C., Williams, W. J., Zimmermann, S., Shimada, K., & Itoh, M. (2009). Joint effects of boundary currents and thermohaline intrusions on the warming of Atlantic water in the Canada Basin, 1993–2007. *Journal of Geophysical Research*, *114*, C00A12. https://doi.org/10.1029/2008JC005001

Meneghello, G., J. Marshall, M.-L. Timmermans, and J. Scott (2018). Observations of seasonal upwelling and downwelling in the Beaufort Sea mediated by sea ice, *Journal of Physical Oceanography*, *48*(4), 795–805. https://doi.org/10.1175/jpo-d-17-0188.1

Meyer, A., Sundfjord, A., Fer, I., Provost, C., Villacieros Robineau, N., Koenig, Z., et al. (2017). Winter to summer oceanographic observations in the Arctic Ocean north of Svalbard. *Journal of Geophysical Research: Oceans*, *122*, 6218–6237. https://doi.org/10.1002/2016jc012391

Nikolopoulos, A., Pickart, R. S., Fratantoni, P. S., Shimada, K., Torres, D. J., & Jones, E. P. (2009). The western Arctic boundary current at 152 W: Structure, variability, and transport. *Deep Sea Research Part II: Topical Studies in Oceanography*, *56*(17), 1164–1181. https://doi.org/10.1016/j.dsr2.2008.10.014

Pérez-Hernández, M. D., Pickart, R. S., Pavlov, V., Våge, K., Ingvaldsen, R., Sundfjord, A. (2017). The Atlantic Water boundary current north of Svalbard in late summer. *Journal of Geophysical Research: Oceans*, *122*, 2269–2290. https://doi.org/10.1002/2016JC012486

Pérez-Hernández, M. D., Pickart, R. S., Torres, D. J., Bahr, F., Sundfjord, A., Ingvaldsen, R., et al. (2019). Structure, transport, and seasonality of the Atlantic Water boundary current north of Svalbard: Results from a yearlong mooring array. *Journal of Geophysical Research: Oceans*, *124*, 1679–1698. https://doi.org/10.1029/2018JC014759

Pickart, R. S., Moore, G., Torres, D. J., Fratantoni, P. S., Goldsmith, R. A., & Yang, J. (2009). Upwelling on the continental slope of the Alaskan Beaufort Sea: Storms, ice, and oceanographic response. *Journal of Geophysical Research*, *114*, C00A13. https://doi.org/10.1029/2008JC005009

Pickart, R. S., Spall, M. A., & Mathis, J. T. (2013). Dynamics of upwelling in the Alaskan Beaufort Sea and associated shelf–basin fluxes. *Deep Sea Research Part I: Oceanographic Research Papers*, *76*, 35–51. https://doi.org/10.1016/j.dsr.2013.01.007

Pickart, R. S., Spall, M. A., Moore, G. W., Weingartner, T. J., Woodgate, R. A., Aagaard, K., & Shimada, K. (2011). Upwelling in the Alaskan Beaufort Sea: Atmospheric forcing and local versus non-local response. *Progress in Oceanography*, *88*(1–4), 78–100. https://doi.org/10.1016/j.pocean.2010.11.005

Pnyushkov, A. V., Polyakov, I. V., Rember, R., Ivanov, V. V., Alkire, M. B., Ashik, I. M., et al. (2018). Heat, salt, and volume transports in the eastern Eurasian Basin of the Arctic Ocean from 2 years of mooring observations. *Ocean Science*, *14*(6), 1349–1371. https://doi.org/10.5194/os-14-1349-2018

Polyakov, I. V. Pnyushkov, A. V., Alkire, M. B., Ashik, I. M., Baumann, T. M., Carmack, E. C., et al. (2017). Greater role for Atlantic inflows on sea-ice loss in the Eurasian Basin of the Arctic Ocean. *Science*, *356*(6335), 285–291. https://doi.org/10.1126/science.aai8204

Regan, H. C., Lique, C., & Armitage, T. W. K. (2019). The Beaufort Gyre extent, shape, and location between 2003 and 2014 from satellite observations. *Journal of Geophysical Research: Oceans*, *124*, 844–862. https://doi.org/10.1029/2018JC014379

Rudels, B., Friedrich H. J., and D. Quadfasel (1999). The Arctic circum- polar boundary current, *Deep-Sea Research, Part II*, *46*, 1023–1062. https://doi.org/10.1016/s0967-0645(99)00015-6

Rudels, B., Jones, E., Anderson, L., & Kattner, G. (1994). On the intermediate depth waters of the Arctic Ocean. In The polar oceans and their role in shaping the global environment, *AGU Geophysical Monograph* (Vol. 85, 33–46). AGU.

Schauer, U., Rudels, B., Jones, E. P., Anderson, L. G., Muench, R. D., Bjork, G., et al. (2002). Confluence and redistribution of Atlantic water in the Nansen, Amundsen and Makarov basins. *Annales de Geophysique*, *20*(2), 257–273. https://doi.org/10.5194/angeo-20-257-2002

Schulze, L. M., and R. S. Pickart, (2012). Seasonal variation of upwelling in the Alaskan Beaufort Sea: Impact of sea ice cover, *Journal of Geophysical Research*, *117*, C06022. https://doi.org/10.1029/2012JC007985

Smith, J. N., Ellis, K. M., & Boyd, T. (1999). Circulation features in the Central Arctic Ocean revealed by nuclear fuel reprocessing tracers from scientific ice expeditions 1995 and 1996. *Journal of Geophysical Research*, *104*(C12), 29663–29677. https://doi.org/10.1029/1999JC900244

Spall, M. A., Pickart, R. S., Fratantoni, P. S., & Plueddemann, A. J. (2008). Western Arctic shelfbreak eddies: Formation and transport. *Journal of Physical Oceanography*, *38*(8), 1644–1668. https://doi.org/10.1175/2007JPO3829.1

Swift, J., Jones, E., Aagaard, K., Carmack, E., Hingston, M., Macdonald, R., et al. (1997). Waters of the Makarov and Canada basins. *Deep Sea Research Part II: Topical Studies in Oceanography*, *44*(8), 1503–1529. https://doi.org/10.1016/S0967-0645(97)00055-6

Våge, K., R. S. Pickart, V. Pavlov, P. Lin, D. J. Torres, R. B. Ingvaldsen, et al. (2016). The Atlantic Water boundary current in the Nansen Basin: Transport and mechanisms of lateral exchange, *Journal of Geophysical Research: Oceans*, *121*, 6946–6960, https://doi.org/10.1002/2016JC011715

Woodgate, R. A., Aagaard, K., Muench, R. D., Gunn, J., Björk, G., Rudels, B., et al. (2001). The Arctic Ocean boundary current along the Eurasian slope and the adjacent Lomonosov Ridge: Water mass properties, transports and transformations from moored instruments. *Deep Sea Research Part I: Oceanographic Research Papers*, *48*(8), 1757–1792. https://doi.org/10.1016/S0967-0637(00)00091-1

Woodgate, R. A., Aagaard, K., Swift, J. H., Smethie, W. M. Jr., & Falkner, K. K. (2007). Atlantic Water circulation over the Mendeleev Ridge and Chukchi Borderland from thermohaline intrusions and water mass properties. *Journal of Geophysical Research*, *112*, C02005. https://doi.org/10.1029/2005JC003416

Zhao, M., M.-L. Timmermans, S. Cole, R. Krishfield, A. Proshutinsky, and J. Toole (2014). Characterizing the eddy field in the Arctic Ocean halocline, *Journal of Geophysical Research: Oceans*, *119*. https://doi.org/10.1002/2014JC010488